

Article

CVD Encapsulation of Laser-Graphitized Electrodes in Diamond Electro-Optical Devices

Maxim S. Komlenok ^{*}, Vitali V. Kononenko , Andrey P. Bolshakov , Nikolay D. Kurochitskiy ,
Dmitrii G. Pasternak , Alexander A. Ushakov  and Vitaly I. Konov

Prokhorov General Physics Institute of the Russian Academy of Sciences, Vavilova Street 38,
Moscow 119991, Russia; kuronick@mail.ru (N.D.K.); dg.pasternak@physics.msu.ru (D.G.P.)

* Correspondence: komlenok@nsc.gpi.ru

Abstract: Conductive graphitized grooves on the dielectric surface of diamond have been created by KrF excimer laser radiation. The advantages of such a circuit board in high-field applications is rather limited because the crystal surface has a relatively low electrical breakdown threshold. To increase the electrical strength, a method of encapsulating surface conductive graphitized structures by chemical vapor deposition of an epitaxial diamond layer has been proposed and realized. The quality of the growth diamond is proved by Raman spectroscopy. A comparative study of the electrical resistivity of graphitized wires and the breakdown fields between them before and after diamond growth was carried out. The proposed technique is crucial for diamond-based high-field electro-optical devices, such as THz photoconductive emitters.

Keywords: diamond; CVD growth; laser-induced graphitization; conductivity; electrical breakdown

1. Introduction

Diamond is a unique material with a number of record-breaking properties. Its electrical breakdown threshold is up to 2–10 MV/cm [1–3], making it attractive for high-voltage applications, such as field electron transistors [4–8], switching diodes [9–13], high-energy particle trapping [14–18], photoconductive antennas [19–22] and others. The thermal conductivity of diamond (24 W/cm·K) [23] is even higher than that of copper, which allows it to effectively dissipate heat [24–28]. Recently, diamond heat sinks have demonstrated high efficiency in reducing the temperature of GaN-based transistors [29]. Diamond has high transparency and radiation resistance over the whole UV-to-mm range, which is used for the fabrication of optics for high-power laser sources [30,31]. The high-quality diamond crystals show excellent transport properties: electron and hole mobilities reach 4500 and 3800 cm²/V·s, respectively, at room temperature [32], and carrier saturation velocity reaches 2.7×10^7 cm/s [33,34]. Another quite important advantage of diamond is the possibility to locally regulate its conductivity. Diamond is an sp³ hybridized carbon allotrope. Its band gap is relatively large (5.4 eV), which makes undoped diamond an excellent insulator: the resistivity of pure crystals can exceed 10¹⁶ Ohm·cm [35]. On the other hand, there is the counterpart of diamond—graphite. It is another sp² hybridized crystalline modification of carbon and normal semimetal. The typical basal plane resistivity of highly oriented pyrolytic graphite (HOPG) is 40 μOhm·cm [36]. Surprisingly, the diamond lattice can be relatively easily transformed into a graphitic lattice by external action. Intense laser radiation is the most suitable and prospective tool to locally modify the carbon structure on the diamond surface or even in the bulk [37–39]. Laser irradiation allows one to create complex conductive patterns in diamond and opens new fields for optical and electronic applications of diamond material. All-carbon detectors of ionized radiation have been fabricated by the laser direct write technique and successfully tested in the registration of β-particles [40]. The same technique has been used to fabricate diamond/graphite metamaterials in the IR [41] and THz [42,43] regions.



Citation: Komlenok, M.S.; Kononenko, V.V.; Bolshakov, A.P.; Kurochitskiy, N.D.; Pasternak, D.G.; Ushakov, A.A.; Konov, V.I. CVD Encapsulation of Laser-Graphitized Electrodes in Diamond Electro-Optical Devices. *Photonics* **2024**, *11*, 10. <https://doi.org/10.3390/photonics11010010>

Received: 10 December 2023

Revised: 19 December 2023

Accepted: 21 December 2023

Published: 23 December 2023



Copyright: © 2023 by the authors. Licensee MDPI, Basel, Switzerland. This article is an open access article distributed under the terms and conditions of the Creative Commons Attribution (CC BY) license (<https://creativecommons.org/licenses/by/4.0/>).

Another application where it is desirable to utilize all of the unique properties of diamond, especially the high electric breakdown field, is THz photoconductive generation. The first diamond-based photoconductive antenna (PCA) was fabricated and tested about 20 years ago [19]. Recently, this field has received a new impetus. Diamond doping allowed the use of commercially available IR fs-laser sources for the optical pumping of PCAs [21,22] instead of the complex UV fs-lasers that would have to be used to generate the photocarriers in pure diamond. However, the demonstrated power of the generated THz radiation is still far from the maximum available. The main limiting factor is that the electrodes forming the E-field in the diamond substrate of the PCA were located on the diamond surface, and the level of the bias voltage was limited by the electrical breakdown on the diamond surface or in air ($E_{\text{surf}} < 20 \text{ kV/cm}$). An obvious solution to dramatically increase the electric field in the PCA is to bury the conductive wires in the substrate. One way of doing this is to create graphitic structures by direct laser writing within the diamond bulk. This technique has been successfully tested and found to be flexible and effective [22]. However, it is mostly limited by the minimum distance between adjacent channels and does not allow the creation of paths with sufficient conductivity [44]. Special efforts should be made to write arbitrary structures and increase their conductivity [45].

In this work, we describe a completely different approach, also using laser microstructuring of diamond. A new two-step technique for fabricating the buried conductive structures has been demonstrated. First, the graphitized wires were produced on the surface of single-crystal diamond by laser ablation, and then they were encapsulated by chemical vapor deposition (CVD) of the diamond layer. It should be mentioned that a similar approach was first realized by Yoneda et al. [2]. They grew the polycrystalline film covering the Pt-patterned diamond surface. Polycrystalline wafers were found to be ineffective in terms of THz generation [21]. Therefore, in this work, we studied the possibility of epitaxially growing single-crystal diamond above the conductive structures.

For the first time, we have investigated the epitaxial growth of a diamond film on a high-pressure, high-temperature (HPHT) substrate with laser-graphitized grooves. There are two main issues to be addressed in the development of encapsulated graphitic electrode technology. Here, we focused on the first, which is the preservation of the electrodes, in particular, the high conductivity of the graphitized material. A gas discharge plasma, which disrupts the methane molecules and provides the diamond growth, is a fairly aggressive environment and is thought to etch all carbon phases including diamond. The preservation of the graphitized material in the CVD process is, therefore, a crucial task, as it is of little value to cover the tracks with an insulating protective layer and at the same time ruin the conductive network and the functionality of the device. The second task is to minimize surface leakage and increase the inter-electrode electrical strength many times over. This is a major task, and a number of possible limitations should be thoroughly investigated, including the thickness of the diamond protective layer, the effect of defect generation in the diamond around the graphitized material [46], etc. Here, we report the first results on this problem by comparing the electrical conductivity and breakdown threshold before and after the CVD encapsulation process.

2. Materials and Methods

Surface graphitization of the HPHT sample was performed using a commercial KrF excimer laser ($\lambda = 248 \text{ nm}$, $\tau = 20 \text{ ns}$) (CL7100, Optosystems Ltd., Moscow, Russia). We chose ns pulse duration for the track formation to increase its conductivity. It is known that the conductivity of the graphitized layer induced by ns-irradiation is larger than that induced by fs-irradiation [47]. The laser beam uniformly illuminated a square mask of $400 \times 400 \mu\text{m}^2$, which was then projected onto the sample surface with a demagnification factor of 1:20 using a homemade objective ($\text{NA} = 0.3$). Laser writing was performed by moving the sample on a three-axis translational stage. The laser spot-ablated the diamond surface to form grooves $24 \mu\text{m}$ wide and $125 \mu\text{m}$ deep, with the graphitized phase at the bottom. Such a deep crater was produced with a laser fluence of 27 J/cm^2 and 400 laser

pulses per spot. A sketch of the graphitized tracks on the diamond surface is shown in Figure 1.

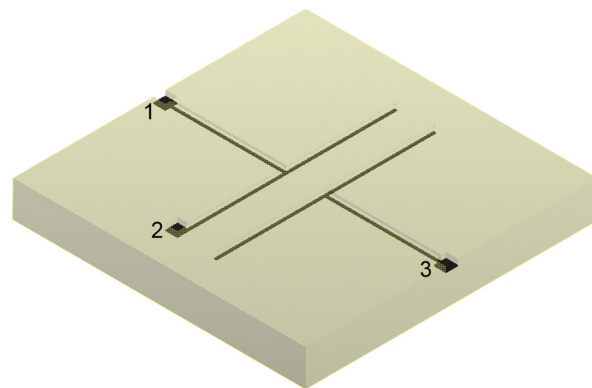


Figure 1. Schematic of graphitized wires with pads (#1, #2, and #3) for measurements of electrical breakdown threshold.

The structure of the graphitized material was analyzed by Raman set-up (Horiba LabRAM HR-800 spectrometer, Kyoto, Japan, equipped with a diode-pumped solid-state laser at $\lambda = 473 \text{ nm}$) in a confocal configuration with a spatial resolution of $1 \mu\text{m}$ and an accuracy of the Raman line position detection down to 0.2 cm^{-1} . The spectrometer was calibrated using a high-quality natural type IIa diamond crystal. The reference spectrum showed the diamond Raman peak at 1332.5 cm^{-1} with a full width at half maximum (FWHM) of 2.9 cm^{-1} . The laser power was 2.2 mW .

The resistivity of the graphitized wires was characterized using a source measure unit (2635B, Keithley, Cleveland, OH, USA). The unit was terminated with two tips attached to the micromanipulators and controlled by an optical microscope. For testing, these tips were touched into $100 \times 100 \mu\text{m}^2$ graphitized pads on the diamond surface (#1 and #2 in Figure 1), providing ohmic contact with the graphitized wires. The inter-electrode electrical strength was studied in air and at room temperature by applying high voltage (HV) to the two $100 \times 100 \mu\text{m}^2$ graphitized pads (#1 and #3 in Figure 1) and using the same tip targeting technique as for the resistivity measurements. The circuit diagram for the breakdown voltage measurements is shown in Figure 2. Electrical breakdown was monitored with a 500 MHz oscillograph (Tektronix, Beaverton, OR, USA). A DC voltage applied by an HV power supply (Stanford Research Systems, Sunnyvale, CA, USA, model PS370) had been increased until a strong leakage current appeared, which was displayed on the oscilloscope as a sharp voltage drop.

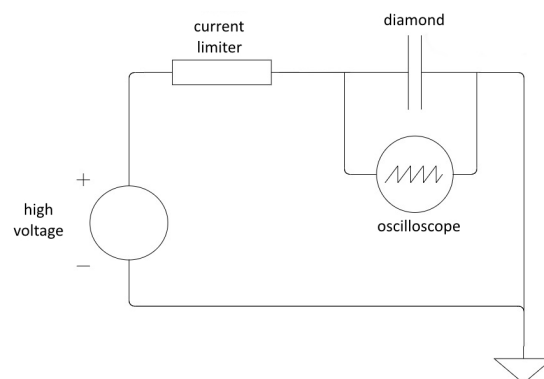


Figure 2. Circuit diagram for breakdown voltage measurements.

Epitaxial growth of a diamond layer on a mechanically polished (100) oriented type Ib commercial (Chenguang Machinery&Electric Equipment Co., Ltd., Changsha, China)

HPHT single crystal substrate of $2.9 \times 2.7 \times 0.4 \text{ mm}^3$ with graphitized tracks was performed using a microwave plasma CVD system ARDIS-300 (Optosystems Ltd., Russia, 6 kW, 2.45 GHz) [48]. The diamond deposition process was carried out at a pressure of 177 Torr, microwave power of 5.1 kW and total flow rate of 500 sccm using a gas mixture of H_2 (96%)/ CH_4 (4%). The substrate temperature of $920 \text{ }^\circ\text{C}$ was maintained during a 5-h deposition run, as measured with a SensorTherm M322 two-color pyrometer at the side of the sample through a special tunnel in the substrate holder. The growth rate during epitaxial growth was monitored using the low-coherence interferometry method. In this method, a device based on a Michelson interferometer records the change in the optical length of the growing crystal (n_d) vs. (t). In the linear parts of the $n_d(t)$ dependence, the tangent of the slope of the line gives the growth rate, which is calculated by the program several times per second, averaged and displayed on the computer monitor. The epitaxial diamond growth rate was about $8 \text{ }\mu\text{m}/\text{hour}$. The thickness of the diamond sample before and after growth was measured with a micrometer screw gauge. By the difference of values, the thickness of the grown layer was calculated, which amounted to $40 \text{ }\mu\text{m}$. After the diamond growth, the surface above the test pads was ablated again with an excimer laser. The epitaxially grown layer was removed to locally open the buried pads and obtain contacts for applying high voltage or controlling the conductivity of the buried wires. The surface morphology was analyzed using an Axiotech 25HD optical microscope (Carl Zeiss, Jena, Germany).

3. Results and Discussion

3.1. Optical Characterization of Laser Structured and Epitaxially Grown Diamond Surface

The optical image of the T-shaped interconnection of graphitized grooves under the grown diamond layer was obtained in the transmission regime of illumination and focusing in depth of material (Figure 3a). The dark stripes correspond to the graphitized structures, which had a width of about $24 \text{ }\mu\text{m}$ (about the same as before the CVD process) and still had a fairly clean edge. Surprisingly, the homogeneity of the diamond layer grown over the grooves was quite high. The image in Figure 3b was obtained by focusing on the diamond surface. The underlying T-shaped intersection of the graphitized grooves is barely visible. Overall, the surface appears perfectly flat—all surface relief features are clearly visible, as they lie within the depth of field of the $50\times$ objective. The epitaxial growth of the groove walls was unexpectedly effective and resulted in closing the gap above the groove. Note the appearance of surface steps perpendicular to the grooves. An obscured T area above the T-connected grooves corresponds to the junction between the diamond crystals grown from opposite walls of the groove. The layers from both walls converge at the junction, forming a shallow groove only a few micrometers deep and about $10 \text{ }\mu\text{m}$ wide. The presence of relief steps on the growth side indicates epitaxial growth of diamond, and they are always formed during epitaxial growth of mosaic diamond on the clean surface and lateral overgrowth of diamond substrates patterned by conventional photolithographic methods [49–51].

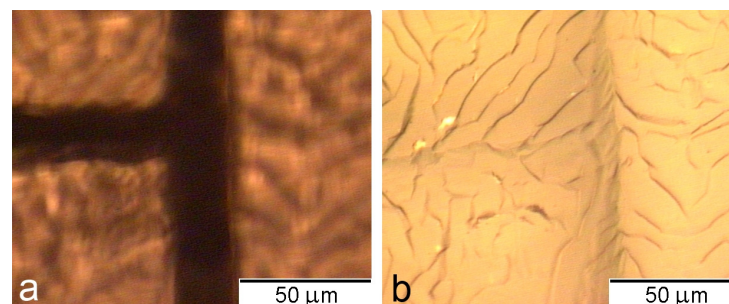


Figure 3. Optical image of the T-connected grooves under the grown diamond layer, obtained in the transmission regime of illumination (a), and the sample surface above the same T-shaped intersection of the grooves (b).

3.2. Confocal Raman Spectroscopy of Deposited Diamond Layer and Encapsulated Graphitized Structures

Raman mapping was used to evaluate the quality of the diamond material in the deposited layer. The obvious critical zone is the vicinity of the graphitized groove and, in particular, the interface between the crystals growing towards each other. The scattered light was collected by focusing on the surface of the grown layer. The Raman spectra were recorded along the direction perpendicular to the junction with a step of $1\ \mu\text{m}$. The position and width of the diamond peak as a function of distance along the scan line are shown in Figure 4a,b, respectively. The scan length was $40\ \mu\text{m}$, and the zero point in Figure 4 corresponds to the position of the junction line. The diamond Raman peak in the obtained spectra was fitted with a Lorentzian line shape to estimate its position and FWHM.

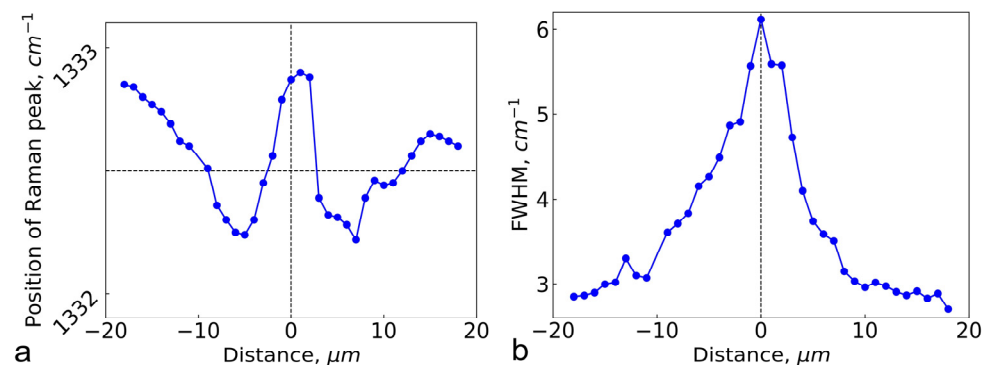


Figure 4. The position (a) and FWHM (b) of the diamond Raman peak as a function of the distance along the scanning line. The vertical dotted line at zero point corresponds to the junction position; horizontal dotted line corresponds to the reference diamond peak position at $1332.5\ \text{cm}^{-1}$.

As the data in Figure 4 show, the Raman peak appeared to be shifted to higher frequencies, up to $1332.9\ \text{cm}^{-1}$, in a zone of about $3\ \mu\text{m}$ width around the junction point. Beyond this range, the peak position decreased to $1332.2\ \text{cm}^{-1}$ in a zone of about $5\ \mu\text{m}$, and so on, forming an oscillation around the reference position of the diamond peak at $1332.5\ \text{cm}^{-1}$. The deviation of the diamond peak position from the reference value is a well-known effect and is caused by mechanical stress, which in turn is a result of structural defects within the grown crystal. The positive shift corresponds to compressive stress and the negative shift corresponds to tensile stress [52].

Thus, Raman spectroscopy reveals strong and localized compressive stress in a $3\ \mu\text{m}$ wide zone around the junction interface and its gradual relaxation extending to about $20\ \mu\text{m}$ outside the junction zone. The Raman peak width (Figure 4b) reaches a maximum value of $6\ \text{cm}^{-1}$ at the junction and then gradually returns to the reference value of $2.9\ \text{cm}^{-1}$. The broadening of the Raman peak is a result of the spatial inhomogeneity of the stress along the scan line direction. The broadening mechanism can be described as follows. Differently strained locations within an analyzed volume result in a number of slightly shifted Raman peaks. The spectrometer detects the superposition of these shifted Raman peaks, causing the inhomogeneous broadening of the Raman line. Thus, the width of the stressed zone around the interface can be estimated from the Raman data to be $\sim 40\ \mu\text{m}$ (Figure 4), which is slightly wider than the gap between the groove walls ($24\ \mu\text{m}$). It is noteworthy that outside the strain region, the Raman spectra of the CVD epitaxial layer show a narrow diamond peak at $1332.5\ \text{cm}^{-1}$ with an FWHM of $2.9\ \text{cm}^{-1}$ (Figure 5), which correspond to the reference values of a high-quality natural type IIa diamond crystal.

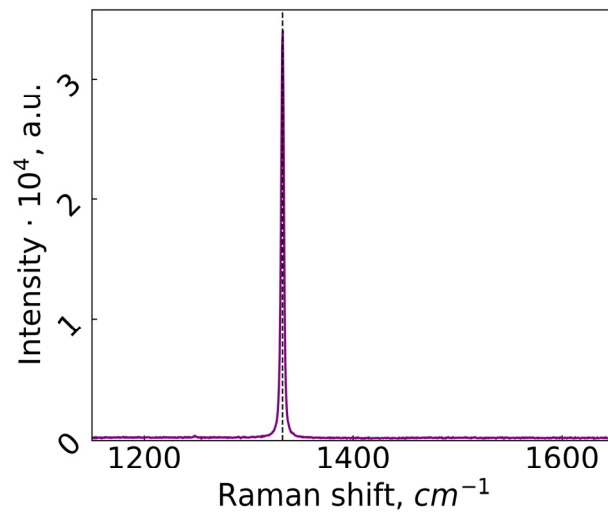


Figure 5. The Raman spectra of the CVD epitaxial diamond layer recorded outside the strain region.

Raman spectroscopy was also used to analyze the structure of the graphitized material. The spectrum of the diamond surface collected after the laser writing presented in Figure 6 (bottom gold dots) shows the typical features of laser-graphitized diamond, commonly attributed to sp^2 -bonded nanocrystalline carbon [53,54]. The two main bands are at 1360 cm^{-1} (D) and 1580 cm^{-1} (G). No signal of the diamond line at 1332 cm^{-1} was detected, as expected, because the modified layer is thick enough and strongly absorbs both the pumping radiation and the scattered signal from the underlying diamond substrate. Using the typical absorption coefficient for graphite, the thickness of the graphitized layer at the bottom of the groove was estimated to be more than 250 nm [55].

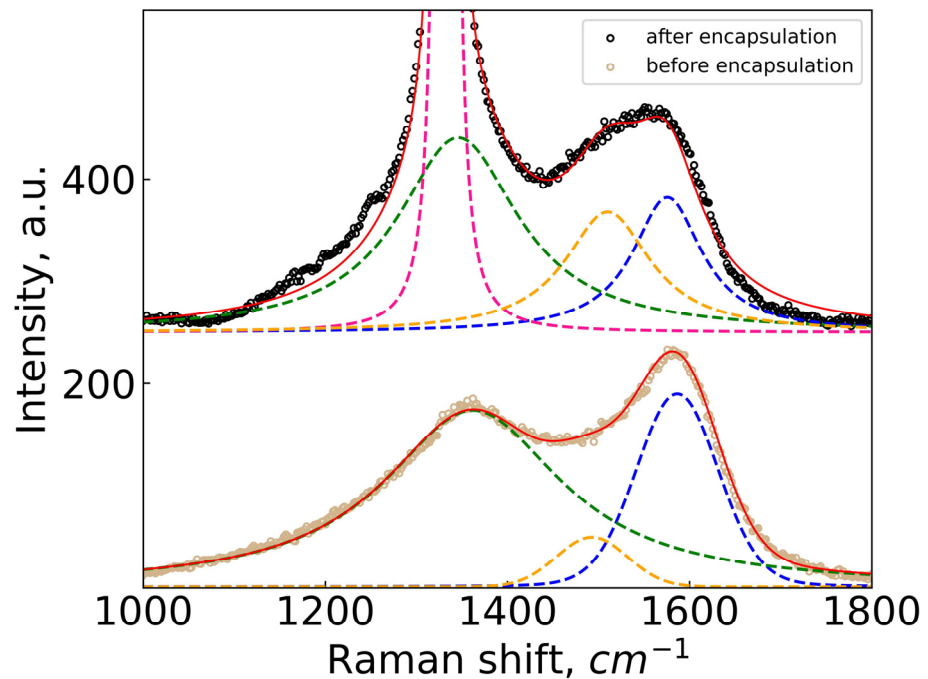


Figure 6. Raman spectra of the graphitized track before (bottom, gold dots) and after (top, black dots) CVD encapsulation. The spectra are shifted vertically for clarity. Experimental spectra were fitted using D-, G-, and A-bands before diamond layer growth and the same bands with the addition of the diamond line after growth. Green dash curves correspond to D-band, blue dash curves correspond to G-band, and gold dash curves correspond to A-band. The red curves correspond to the resulting fitting spectra.

After CVD encapsulation, the Raman spectrum of the graphitized phase was recorded by focusing the microscope objective on the dark structures as shown in Figure 3a. The typical spectrum is illustrated by the black dots in Figure 6. The pump radiation has passed through the epitaxial layer, and the significant part of the Raman signal comes from the diamond. The diamond line at 1332 cm^{-1} was so strong that it masked the D-band centered at 1360 cm^{-1} . The appearance of a strong red wing belonging to the G-band is also clearly seen. Such behavior usually results from the appearance of an additional band between D and G, located at about 1500 cm^{-1} . This band, called the “A-band” [56], is attributed to the out-of-plane graphitic defects [57]. It is often found in laser-graphitized diamond [58], but the typical A-band intensity is rather low, as in the spectra prior to diamond layer growth. The reason for the remarkable enhancement of this band after CVD growth is unclear.

In general, we did not observe any valuable changes in the Raman spectrum after encapsulation of the graphitized layer, which could affect the conductivity of the laser-induced wires. The G peak remained stable; neither narrowing nor broadening, which could indicate the ordering or disordering of the graphite structure, were found. The alternative way to follow the amplitude ratio of D and G bands also could not be realized because of the masking of the D band.

3.3. Electrical Conductivity of Encapsulated Graphitized Structures

As emphasized above, a key requirement for the developed technology is the high conductivity of the graphitized phase retained during the encapsulation process. Although Raman spectroscopy did not reveal structural changes in the sp^2 phase and thus in the track conductivity, direct electrical tests showed a remarkable difference. The current–voltage curves measured between points #1 and #2 of the graphitized wire (see Figure 1) before and after encapsulation are shown in Figure 7. A large improvement in conductivity was observed after epitaxial diamond growth. The resistivity dropped from 6.6 to 4.6 $\text{m}\Omega\text{ cm}$. The possible explanation for this effect is the modification of the nanocrystalline sp^2 phase at high temperature of the $\text{H}_2(96\%)/\text{CH}_4(4\%)$ gas mixture in the plasma reactor. It should be noted that the resistivity of the original track calculated from the presented data was quite close to those previously reported after graphitization of the diamond surface by nanosecond laser pulses [47].

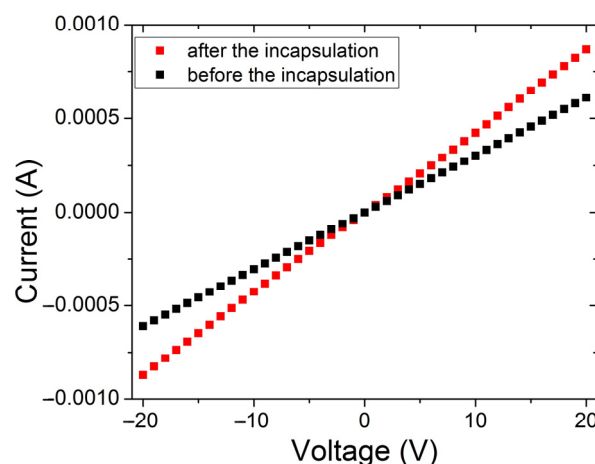


Figure 7. The current–voltage characteristics of the graphitized track before and after the CVD diamond encapsulation.

3.4. Electrical Strength between Encapsulated Graphitized Structures

First, the interelectrode voltage was measured immediately after laser structuring of the diamond surface. A gradually increasing DC voltage was applied at a distance of 300 μm between pads #1 and #3 (Figure 1), monitoring the jump of the leakage currents. The maximum value of the DC voltage withstood by the surface capacitance of the diamond

was found to be 1.2 kV. At the given 300 μm inter-electrode spacing, the breakdown field was calculated to be 40 kV/cm. Note, however, that the shortest distance between the conductive wires can be much larger. The depth of each groove, which is 125 μm , should be taken into account. Then, the total distance between the conductive structures is about 550 μm and the corresponding breakdown field reaches ~ 22 kV/cm. The range of 22 kV/cm to 40 kV/cm covers the known value of 30 kV/cm for air, which in turn is not exact and can vary depending on electrode geometry, electrode roughness, humidity, and other environmental conditions [59].

After deposition of the 40 μm diamond layer, the breakdown voltage increased to 3.4 kV. In this case, however, the discharge took place over the surface of the diamond. The sparks were observed between the two opened graphitized pads #2 and #3 separated by 1.8 mm (see Figure 1). The breakdown field over this surface distance was calculated to be approximately 19 kV/cm, which is close to the surface measurements above. To estimate the breakdown threshold for bulk diamond, the circuit diagram describing different paths of electrical discharge should be considered (Figure 8).

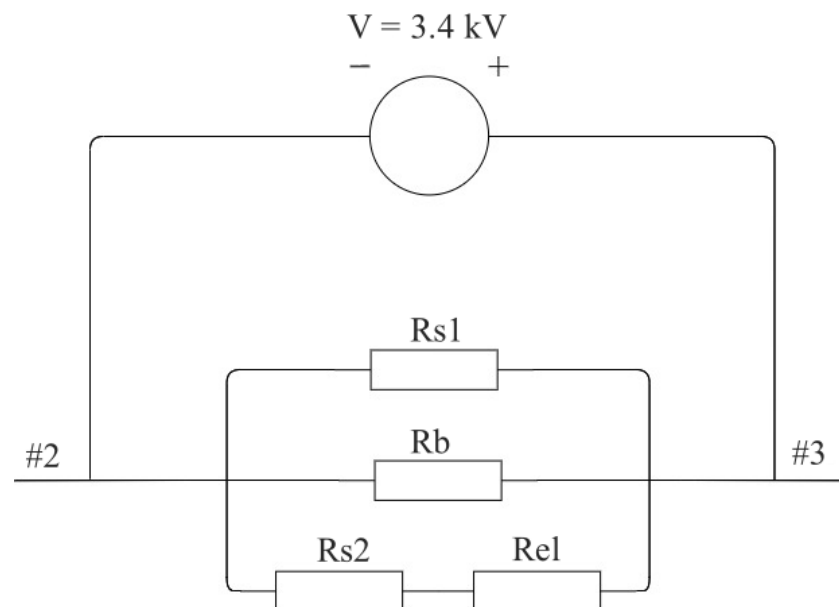


Figure 8. The circuit diagram describing different paths of electrical discharge between the pads #2 and #3. R_{s1} and R_{s2} correspond to the diamond surface resistance over the distance of 1.8 mm and 550 μm , respectively. R_b corresponds to the resistance over a 300 μm gap in the bulk diamond. R_{el} corresponds to the resistance over a 40 μm thick grown epitaxial diamond layer.

There are three possible pathways of electrical breakdown between the pads #2 and #3. The first two are obvious: the first path, 1.8 mm long, is through the diamond surface and is labeled R_{s1} ; the second path is through a 300 μm gap in the bulk diamond and is labeled R_b . The third path is more puzzling; this path passes sequentially through a 550 μm long diamond surface (R_{s2}) and a 40 μm thick grown epitaxial diamond layer (R_{el}). The lower estimates of the electrical strength can be deduced from the absence of breakdown through the second and third paths at the applied voltage of 3.4 kV. For the second path, the breakdown threshold can be calculated as $3.4 \text{ kV}/300 \mu\text{m} \approx 110 \text{ kV/cm}$. In the third case, the voltage of 3.4 kV is applied to the elements R_{s2} and R_{el} connected in series in a circuit. Since we did not observe a short circuit, the voltage across R_{s2} was below 1.2 kV, which was previously determined as the surface threshold. Thus, the voltage across R_{el} was above $3.4 - 1.2 = 2.2 \text{ kV}$, and the lower estimate of the breakdown threshold for the deposited diamond layer was at least $2.2 \text{ kV}/40 \mu\text{m} = 550 \text{ kV/cm}$.

4. Conclusions

In conclusion, this work reported the first attempt to encapsulate the graphitized structures produced by a nanosecond laser on a single crystal diamond substrate using chemical vapor deposition. The 40 μm epitaxial diamond layer was found to completely cover both the original and the graphitized surface. Raman spectroscopy proved the quality of the synthesized monocrystalline layer and indicated the stress in the joint area of about 40 μm width, which was slightly wider than the gap between the groove walls (24 μm). A comparative study of graphitized wires before and after the encapsulation process showed not only the preservation of the conductive properties of the laser-graphitized phase, but surprisingly even some improvement in conductivity, which was tentatively attributed to the high-temperature annealing of the nanographite phase. The lower estimate of the electrical breakdown field measured between two encapsulated wires gave 550 kV/cm, which is certainly less than the reference value for diamond (2 MV/cm), but encourages the next steps towards increasing the electrical strength in HV diamond-based devices. Future work should focus on the quality of the epitaxial layer, its compliance with the parameters of laser-graphitized wires, and testing the emissive properties of a THz photoconductive antenna with CVD-encapsulated electrodes.

Author Contributions: Conceptualization, M.S.K. and V.V.K.; methodology, M.S.K.; validation, N.D.K.; investigation, A.P.B., N.D.K. and D.G.P.; data curation, N.D.K.; writing—original draft preparation, M.S.K.; writing—review and editing, M.S.K. and V.V.K.; visualization, N.D.K. and D.G.P.; supervision, V.I.K.; project administration, A.A.U.; funding acquisition, A.A.U. All authors have read and agreed to the published version of the manuscript.

Funding: This research was funded by Ministry of Science and Higher Education of the Russian Federation, grant number 075-15-2020-790.

Institutional Review Board Statement: Not applicable.

Informed Consent Statement: Not applicable.

Data Availability Statement: Data available on request.

Conflicts of Interest: The authors declare no conflict of interest.

References

1. Geis, M.W. Growth of Device-Quality Homoepitaxial Diamond Thin Films. *MRS Online Proc. Libr.* **1989**, *162*, 15–22. [[CrossRef](#)]
2. Yoneda, H.; Ueda, K.I.; Aikawa, Y.; Baba, K.; Shohata, N. Photoconductive properties of chemical vapor deposited diamond switch under high electric field strength. *Appl. Phys. Lett.* **1995**, *66*, 460–462. [[CrossRef](#)]
3. Bogdanov, A.V. Investigation of microplasma breakdown at a contact between a metal and a semiconducting diamond. *Sov. Phys. Semicond* **1982**, *16*, 720.
4. Aleksov, A.; Kubovic, M.; Kaeb, N.; Spitzberg, U.; Bergmaier, A.; Dollinger, G.; Bauer, T.; Schreck, M.; Stritzker, B.; Kohn, E. Diamond field effect transistors—Concepts and challenges. *Diam. Relat. Mater.* **2023**, *12*, 391–398. [[CrossRef](#)]
5. Saha, N.C.; Kim, S.W.; Oishi, T.; Kasu, M. 3326-V modulation-doped diamond MOSFETs. *IEEE Electron Device Lett.* **2022**, *43*, 1303–1306. [[CrossRef](#)]
6. Araujo, D.; Suzuki, M.; Lloret, F.; Alba, G.; Villar, P. Diamond for electronics: Materials, processing and devices. *Materials* **2021**, *14*, 7081. [[CrossRef](#)]
7. Zhang, M.; Wei, W.; Chen, G.; Wen, F.; Lin, F.; He, S.; Wang, Y.; Zhang, L.; Fan, S.; Bu, R.; et al. Electrical properties of cerium hexaboride gate hydrogen-terminated diamond field effect transistor with normally-off characteristics. *Carbon* **2023**, *201*, 71–75. [[CrossRef](#)]
8. He, S.; Chen, G.; Han, X.; Wang, W.; Chang, X.; Li, Q.; Zhang, Q.; Wang, Y.-F.; Zhang, M.; Zhu, T.; et al. Solution-processed tin oxide thin film for normally-off hydrogen terminated diamond field effect transistor. *Appl. Phys. Lett.* **2022**, *120*, 132102. [[CrossRef](#)]
9. Dang, C.; Lu, A.; Wang, H.; Zhang, H.; Lu, Y. Diamond semiconductor and elastic strain engineering. *J. Semicond.* **2022**, *43*, 021801. [[CrossRef](#)]
10. Ghosh, S.; Surdi, H.; Kargar, F.; Koeck, F.A.; Rumyantsev, S.; Goodnick, S.; Nemanich, R.J.; Balandin, A.A. Excess noise in high-current diamond diodes. *Appl. Phys. Lett.* **2022**, *120*, 062103. [[CrossRef](#)]
11. Cañas, J.; Eon, D. Barrier height requirements for leakage suppression in diamond power Schottky diodes. *Diam. Relat. Mater.* **2023**, *136*, 110038. [[CrossRef](#)]

12. Weippert, J.; Reinke, P.; Benkhelifa, F.; Czap, H.; Giese, C.; Kirste, L.; Straňák, P.; Kustermann, J.; Engels, J.; Lebedev, V. Pseudovertical Schottky Diodes on Heteroepitaxially Grown Diamond. *Crystals* **2022**, *12*, 1626. [[CrossRef](#)]
13. Marinelli, M.; Milani, E.; Paoletti, A.; Tucciarone, A.; Verona-Rinati, G.; Angelone, M.; Pillon, M. Trapping and detrapping effects in high-quality chemical-vapor-deposition diamond films: Pulse shape analysis of diamond particle detectors. *Phys. Rev. B* **2001**, *64*, 195205. [[CrossRef](#)]
14. Ramos, M.R.; Crnjac, A.; Cosic, D.; Jakšić, M. Ion microprobe study of the polarization quenching techniques in single crystal diamond radiation detectors. *Materials* **2022**, *15*, 388. [[CrossRef](#)] [[PubMed](#)]
15. Edoardo, B.; Nicola, M. Diamond Detectors for Timing Measurements in High Energy Physics. *Front. Phys.* **2020**, *8*, 248.
16. Liu, Y.-H.; Loh, C.-W.; Zhang, J.-L.; Wu, F.-L.; Qi, M.; Hei, L.-F.; Lv, F.-X.; Lv, Y.-L.; Ge, T.; Li, Y.-Q.; et al. Proton irradiation tests of single crystal diamond detector at CIAE. *Nucl. Mater. Energy* **2020**, *22*, 100735. [[CrossRef](#)]
17. Anderlini, L.; Bellini, M.; Cindro, V.; Corsi, C.; Kanxheri, K.; Lagomarsino, S.; Lucarelli, C.; Morozzi, A.; Passaleva, G.; Passeri, D.; et al. A Study of the Radiation Tolerance and Timing Properties of 3D Diamond Detectors. *Sensors* **2022**, *22*, 8722. [[CrossRef](#)]
18. Chiodini, G.; Martino, M. Diamond Radiation Detectors. *Photocond. Photocond. Mater. Fundam. Tech. Appl.* **2022**, *2*, 689–714.
19. Yoneda, H.; Tokuyama, K.; Ueda, K.-I.; Yamamoto, H.; Baba, K. High power terahertz radiation with diamond photoconductive antenna array. In Proceedings of the 25th International Conference on Infrared and Millimeter Waves (Cat. No. 00EX442), Beijing, China, 12–15 September 2000; pp. 61–62.
20. Yoneda, H.; Tokuyama, K.; Ueda, K.-I.; Yamamoto, H.; Baba, K. High-power terahertz radiation emitter with a diamond photoconductive switch array. *Appl. Opt.* **2011**, *40*, 6733–6736. [[CrossRef](#)]
21. Kononenko, V.V.; Komlenok, M.S.; Chizhov, P.A.; Bukin, V.V.; Bulgakova, V.V.; Khomich, A.A.; Bolshakov, A.P.; Konov, V.I.; Garnov, S.V. Efficiency of Photoconductive Terahertz Generation in Nitrogen-Doped Diamonds. *Photonics* **2022**, *9*, 18. [[CrossRef](#)]
22. Kononenko, T.V.; Ashikkalieva, K.K.; Kononenko, V.V.; Zavedeev, E.V.; Dezhkina, M.A.; Komlenok, M.S.; Ashkinazi, E.E.; Bukin, V.V.; Konov, V.I. Diamond Photoconductive Antenna for Terahertz Generation Equipped with Buried Graphite Electrodes. *Photonics* **2023**, *10*, 75. [[CrossRef](#)]
23. Yamamoto, Y.; Imai, T.; Tanabe, K.; Tsuno, T.; Kumazawa, Y.; Fujimori, N. The measurement of thermal properties of diamond. *Diamond Rel. Mater.* **1997**, *6*, 1057–1061.
24. Fu, J.; Hoffman, A.; Kuntumalla, M.K.; Wang, H.-X.; Chen, D.; Mosyak, A.; Yossifon, G. Investigation of the cooling enhancement of a single crystal diamond heat sink with embedded microfluidic channels. *Diam. Relat. Mater.* **2022**, *130*, 109470. [[CrossRef](#)]
25. Hao, X.; Liu, B.; Li, Y.; Zhao, J.; Zhang, S.; Wen, D.; Liu, K.; Dai, B.; Han, J.; Zhu, J. Diamond single crystal-polycrystalline hybrid microchannel heat sink strategy for directional heat dissipation of hot spots in power devices. *Diam. Relat. Mater.* **2023**, *135*, 109858. [[CrossRef](#)]
26. Du, L.; Yuan, J.; Deng, N.; Qu, Y.; Zhang, X.; Hu, W. Heat transfer properties of single crystal diamond zigzag double-layer microchannel heat sinks. *Int. J. Therm. Sci.* **2024**, *196*, 108687. [[CrossRef](#)]
27. Zhang, C.; Vispute, R.D.; Fu, K.; Ni, C. A review of thermal properties of CVD diamond films. *J. Mater. Sci.* **2023**, *58*, 3485–3507. [[CrossRef](#)]
28. Negmatov, S.S.; Daminov, A.A.; Umarov, A.V.; Abed, N.S.; Berkinov, E.H. Synthetic Diamond Thermistors and Heatsinks. *J. Optoelectron. Laser* **2022**, *41*, 764–769.
29. Mu, F.; He, R.; Suga, T. Room temperature GaN-diamond bonding for high-power GaN-on-diamond devices. *Scr. Mater.* **2018**, *150*, 148–151. [[CrossRef](#)]
30. Kononenko, V.V.; Konov, V.I.; Pimenov, S.M.; Prokhorov, A.M.; Pavel'ev, V.S.; Soifer, V.A. Diamond diffraction optics for CO₂ lasers. *Quantum Electron.* **1999**, *29*, 9. [[CrossRef](#)]
31. Komlenok, M.; Kononenko, T.; Sovyk, D.; Pavelyev, V.; Knyazev, B.; Ashkinazi, E.; Reshetnikov, A.; Komandin, G.; Pashinin, V.; Ralchenko, V.; et al. Diamond diffractive lens with a continuous profile for powerful terahertz radiation. *Opt. Lett.* **2021**, *46*, 340–343. [[CrossRef](#)]
32. Isberg, J.; Hammersberg, J.; Johansson, E.; Wikström, T.; Twitchen, D.J.; Whitehead, A.J.; Coe, S.N.; Scarsbrook, G.A. High carrier mobility in single-crystal plasma-deposited diamond. *Science* **2002**, *297*, 1670–1672. [[CrossRef](#)] [[PubMed](#)]
33. Kalish, R. Diamond as a unique high-tech electronic material: Difficulties and prospects. *J. Phys. D Appl. Phys.* **2007**, *40*, 6467. [[CrossRef](#)]
34. Wort, C.J.H.; Balmer, R.S. Diamond as an electronic material. *Mater. Today* **2008**, *11*, 22–28. [[CrossRef](#)]
35. Field, E. *The Properties of Diamond*; Academic Press: London, UK, 1979; pp. 82, 389 and 652.
36. Marchand, D.; Fretigny, C.; Lagues, M.; Legrand, A.P.; McRae, E.; Mareche, J.F.; Lelaurain, M. Surface structure and electrical conductivity of natural and artificial graphites. *Carbon* **1984**, *22*, 497–506.
37. Fedoseev, D.V.; Varshavskaya, I.G.; Lavrent'ev, A.V.; Deryaguin, B.V. Phase transformations in highly disperse powders during their rapid heating and cooling. *Powder Technol.* **1985**, *44*, 125–129. [[CrossRef](#)]
38. Rothschild, M.; Arnone, C.; Ehrlich, D.J. Excimer-laser etching of diamond and hard carbon films by direct writing and optical projection. *J. Vac. Sci. Technol. B Microelectron. Process. Phenom.* **1986**, *4*, 310–314. [[CrossRef](#)]
39. Kononenko, T.V.; Meier, M.; Komlenok, M.S.; Pimenov, S.M.; Romano, V.; Pashinin, V.P.; Konov, V.I. Microstructuring of diamond bulk by IR femtosecond laser pulses. *Appl. Phys. A* **2008**, *90*, 645–651. [[CrossRef](#)]
40. Lagomarsino, S.; Bellini, M.; Corsi, C.; Gorelli, F.; Parrini, G.; Santoro, M.; Sciortino, S. Three-dimensional diamond detectors: Charge collection efficiency of graphitic electrodes. *Appl. Phys. Lett.* **2013**, *103*, 233507. [[CrossRef](#)]

41. Kononenko, T.; Dyachenko, P.; Konov, V. Diamond photonic crystals for the IR spectral range. *Opt. Lett.* **2014**, *39*, 6962–6965. [[CrossRef](#)]
42. Shimizu, M.; Shimotsuma, Y.; Sakakura, M.; Yuasa, T.; Homma, H.; Minowa, Y.; Tanaka, K.; Miura, K.; Hirao, K. Periodic metallo-dielectric structure in diamond. *Opt. Express* **2009**, *17*, 46–54. [[CrossRef](#)]
43. Komlenok, M.S.; Lebedev, S.P.; Komandin, G.A.; Piqué, A.; Konov, V.I. Fabrication and electrodynamic properties of all-carbon terahertz planar metamaterials by laser direct-write. *Laser Phys. Lett.* **2018**, *15*, 036201. [[CrossRef](#)]
44. Lagomarsino, S.; Bellini, M.; Corsi, C.; Fanetti, S.; Gorelli, F.; Liontos, I.; Parrini, G.; Santoro, M.; Sciortino, S. Electrical and Raman-imaging characterization of laser-made electrodes for 3D diamond detectors. *Diam. Relat. Mater.* **2014**, *43*, 23–28. [[CrossRef](#)]
45. Sun, B.; Salter, P.S.; Booth, M.J. High conductivity micro-wires in diamond following arbitrary paths. *Appl. Phys. Lett.* **2014**, *105*, 231105. [[CrossRef](#)]
46. Pimenov, S.M.; Vlasov, I.I.; Khomich, A.A.; Neuenschwander, B.; Muralt, M.; Romano, V. Picosecond-laser-induced structural modifications in the bulk of single-crystal diamond. *Appl. Phys. A* **2011**, *105*, 673–677. [[CrossRef](#)]
47. Komlenok, M.S.; Dezhkina, M.A.; Kononenko, V.V.; Khomich, A.A.; Popovich, A.F.; Konov, V.I. Effect of laser radiation parameters on the conductivity of structures produced on the polycrystalline diamond surface. *Bull. Lebedev Phys. Inst.* **2017**, *44*, 246–248. [[CrossRef](#)]
48. Available online: <https://optosystems.ru/> (accessed on 12 December 2023).
49. Wang, Y.F.; Chang, X.; Liu, Z.; Liu, Z.; Fu, J.; Zhao, D.; Shao, G.; Wang, J.; Zhang, S.; Liang, Y.; et al. Lateral overgrowth of diamond film on stripes patterned Ir/HPHT-diamond substrate. *J. Cryst. Growth* **2018**, *489*, 51–56. [[CrossRef](#)]
50. Fu, J.; Liu, Z.; Zhu, T.; Zhang, M.; Zhang, X.; Shao, G.; Liu, Z.; Wang, Y.; Zhao, D.; Chang, X.; et al. Fabrication of microchannels in single crystal diamond for microfluidic systems. *Microfluid. Nanofluidics* **2018**, *22*, 92. [[CrossRef](#)]
51. Zhu, X.; Liu, J.; Shao, S.; Tu, J.; Huang, Y.; Bi, T.; Chen, L.; Wei, J.; Kawarada, H.; Li, C. Evolution of growth characteristics around the junction in the mosaic diamond. *Diam. Relat. Mater.* **2021**, *120*, 108640. [[CrossRef](#)]
52. Tardieu, A.; Cansell, F.; Petitet, J.P. Pressure and temperature dependence of the first-order Raman mode of diamond. *J. Appl. Phys.* **1990**, *68*, 3243–3245. [[CrossRef](#)]
53. Lespade, P.; Al-Jishi, R.; Dresselhaus, M.S. Model for Raman scattering from incompletely graphitized carbons. *Carbon* **1982**, *20*, 427. [[CrossRef](#)]
54. Ferrari, A.C.; Robertson, J. Interpretation of Raman spectra of disordered and amorphous carbon. *Phys. Rev. B* **2000**, *61*, 14095. [[CrossRef](#)]
55. Komlenok, M.S.; Dezhkina, M.A.; Khomich, A.A.; Orekhov, A.S.; Orekhov, A.S.; Konov, V.I. Measuring the Local Thickness of Laser-Induced Graphitized Layer on Diamond Surface by Raman Spectroscopy. *Phys. Status Solidi B* **2019**, *256*, 1800686. [[CrossRef](#)]
56. Merlen, A.; Buijnsters, J.G.; Pardanaud, C. A guide to and review of the use of multiwavelength Raman spectroscopy for characterizing defective aromatic carbon solids: From graphene to amorphous carbons. *Coatings* **2017**, *7*, 153. [[CrossRef](#)]
57. Benybassez, C.; Rouzaud, J.N. Characterization of carbonaceous materials by correlated electron and optical microscopy and raman microspectroscopy. *Scan. Electr. Microsc.* **1985**, *1*, 119–132.
58. Khomich, A.A.; Kononenko, V.; Kudryavtsev, O.; Zavedeev, E.; Khomich, A.V. Raman study of the diamond to graphite transition induced by the single femtosecond laser pulse on the (111) face. *Nanomaterials* **2023**, *13*, 162. [[CrossRef](#)]
59. Hong, A. Dielectric Strength of Air. *The Physics Factbook*. 2000. Available online: <https://hypertextbook.com/facts/2000/AliceHong.shtml> (accessed on 12 December 2023).

Disclaimer/Publisher’s Note: The statements, opinions and data contained in all publications are solely those of the individual author(s) and contributor(s) and not of MDPI and/or the editor(s). MDPI and/or the editor(s) disclaim responsibility for any injury to people or property resulting from any ideas, methods, instructions or products referred to in the content.